Polyaromatic Units Set the Albedo of Dark Extraterrestrial Materials

Romain Maupin, Zahia Djouadi, Rosario Brunetto, Obadias Mivumbi, Christophe Sandt, Ferenc Borondics

Polyaromatic Units Set the Albedo of Dark Extraterrestrial Materials

Romain Maupin[1] , Zahia Djouadi[1], Rosario Brunetto[1] , Obadias Mivumbi[1], Christophe Sandt[2], and Ferenc Borondics[2]

[1] Université Paris-Saclay CNRS, Institut d'Astrophysique Spatiale, F-91405, Orsay, France; zahia.djouadi@universite-paris-saclay.fr
[2] Synchrotron SOLEIL, BP48, L'Orme des Merisiers, Gif-sur-Yvette, Cedex, 91192, France
Received 2021 May 17; revised 2021 December 8; accepted 2021 December 10; published 2022 January 20

Abstract

Primitive extraterrestrial materials are generally dark, a characteristic often associated with the presence of polyaromatic organic material and/or sulfides. We show in this study that the reflectance level measured at 0.55 μm of IDPs and some meteorites is correlated to the degree of graphitization of the polyaromatic organic matter. The reflectance level of the primitive surfaces therefore allows us to obtain information on the polyaromatic organic material present on the surface of solar system small bodies observed by remote sensing or visited by space missions. We discuss our results in view of the sample return missions Hayabusa2 and OSIRIS-REx.

Unified Astronomy Thesaurus concepts: Experimental techniques (2078); Spectroscopy (1558); Infrared observatories (791); Interplanetary dust (821); Meteorites (1038); Asteroids (72); Comets (280)

1. Introduction

Asteroid and comet studies and exploration allow us to go back to the origins, formation, and evolution of our solar system. The most primitive of these small bodies, comets and C-, P-, and D-type asteroids, (Vernazza et al. 2015) are often the darkest ones, characterized by a low albedo $\leqslant$10% (Vernazza & Beck 2016; Dumas et al. 1998). Their low albedo is often associated with the presence of organic matter and/or sulfides on their surfaces (Quirico et al. 2016); it could also be due to an effect of grain size (Greenberg 1986). These objects are very interesting from an astrochemical and astrobiological point of view but are particularly difficult to observe due to their low albedo. The spectral study of dark surfaces of the solar system mainly relies on spectral slopes and the reflectance level in the visible and near-infrared (Vis–NIR) range. However, these two parameters do not provide unambiguous chemical information since different materials can have similar absorption properties without having the same chemical composition or the same physical characteristics (grain size, roughness). Laboratory analyses of terrestrial materials and/or extraterrestrial samples available on Earth as analogs of these dark surfaces can help constrain the spectral properties of these objects.

Besides meteorites, it is possible to access to a large amount of extraterrestrial matter on Earth: about 40,000 tons of material fall into Earth's atmosphere every year (Love & Brownlee 1993), mostly in the form of dust called interplanetary dust particles (IDPs), which have been collected in the stratosphere by NASA since 1981. IDPs are primitive extraterrestrial materials originating from asteroids and comets, in most cases not sampled by meteorites (e.g., Vernazza et al. 2015 and references therein); they allow the study of the physicochemical properties of primitive small bodies in the laboratory. Even if the unambiguous identification of the parent bodies of the studied IDPs in the laboratory remains difficult, the fact that they originate from asteroids and comets makes it possible to extract valuable information on the chemical properties of solar system dark surfaces.

Infrared (IR) spectroscopy has long been used to study IDPs and extraterrestrial materials in general, since it is a nondestructive analytical technique for obtaining chemical and mineralogical information. Silicates are the major mineral component; they allow us to distinguish three groups of IDPs: olivine-rich IDPs, pyroxene-rich IDPs, and layer lattice silicate-rich ones (Sandford & Bradley 1989). Most IDPs have elemental abundances approximating those of carbonaceous chondrites, conversely to nonchondritic ones (Rietmeijer 1998). IDPs are generally classified into two groups: chondritic porous IDPs (CP-IDPs) and chondritic smooth IDPs (CS-IDPs). The CP-IDPs have a porosity as high as 70% and a mineralogy dominated by anhydrous silicates (pyroxene and/or olivine) while CS-IDPs are characterized by platy and/or fibrous surface textures and a mineralogy characterized by hydrated silicates (Bradley 2003). IDPs also contain a large amount of organic matter (Thomas et al. 1993; Flynn et al. 2003) composed of aromatic and aliphatic compounds (e.g., Clemett et al. 1993; Matrajt et al. 2012 and references therein). Spectroscopic studies do not show exact similitude between the structure of the polyaromatic material of IDPs and those of primitive chondrites (Martins et al. 2020). Chemical composition of IDPs can be influenced by the thermal and/or irradiation processes they have experienced. Thermal annealing changes the amount of aliphatic organic matter in favor of aromatic matter (Goto et al. 2000). The heating undergone by some IDPs during their atmospheric entry can also cause the destruction of the aliphatic component (Battandier et al. 2018). Irradiation also modifies the degree of disorder of the aromatic material and destroys the aliphatic chains (Muñoz Caro et al. 2006).

Few studies have investigated the Vis–NIR reflectance spectroscopy of IDPs due to their small size (Bradley et al. 1996 and Maupin et al. 2020). By coupling reflectance studies with other analytical techniques, it is possible to investigate possible links between chemical composition and Vis–NIR spectral properties on direct analogs of solar system dark surfaces.

In this study we combined different spectroscopic analyses to study 8 IDPs and 4 different meteorites of CM, CO, and
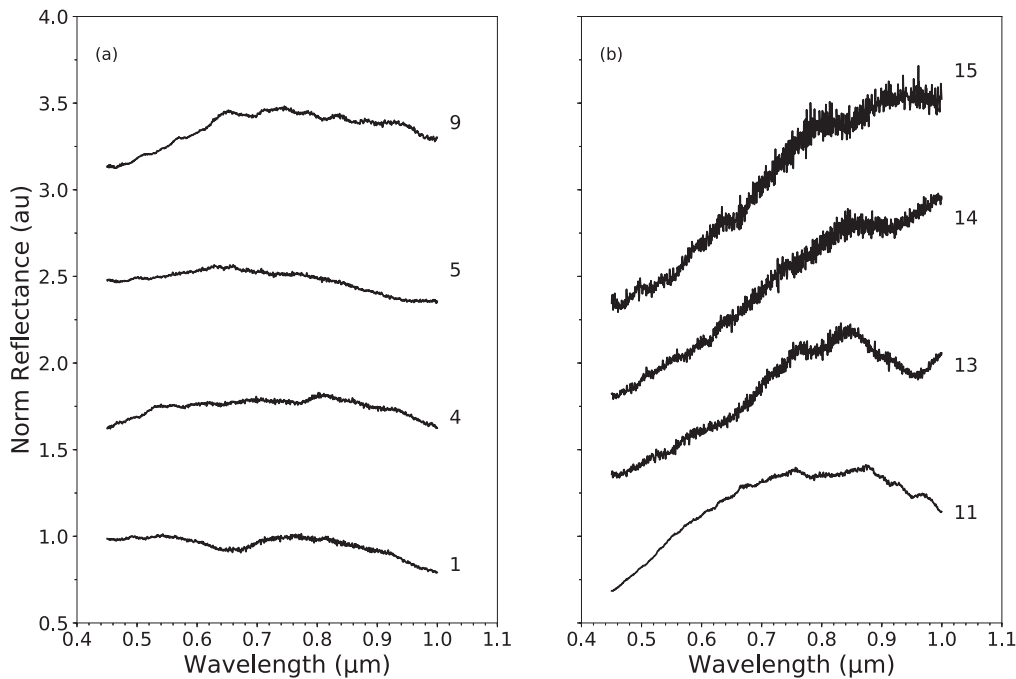
Figure 1. The Vis–NIR reflectance spectra of the studied IDPs. The allocated number for each IDP (see Table 1) is indicated above its spectrum. The spectra are shifted in the reflectance axis for clarity. For more details on how these spectra have been obtained, see Maupin et al. (2020).

Table 1
Vis–NIR Reflectance Level of the Studied Samples

Particle	Allocated Number	Reflectance Level (%)
L2079C18	1	6.1 ± 0.5
W7068B18	4	3.3 ± 0.6
L2071E34	5	2.7 ± 0.3
L2079D12	9	4.2 ± 0.7
L2071E43	11	5.8 ± 0.4
L2083G23[*]	13	2.6 ± 0.7
W7068B37	14	2.9 ± 0.6
L2083E39	15	1.2 ± 0.5
Frontier Mountain	…	15.0 ± 0.3
Allende	…	8.1 ± 0.8
Murchisson	…	3.2 ± 0.9
Tagish Lake[a]	…	2.4 ± 0.8

Note. The reflectance levels of the studied IDPs from (Maupin et al. 2020). [*] indicates cosmic particle. [a] The value of reflectance for Tagish Lake is from Beck et al. (2012).

CV-type. We used the Vis–NIR spectroscopy in the range (0.45–1.0 μm), the mid-IR spectroscopy in the range (2.5–15 μm) as well as Raman microspectroscopy to obtain information on the minerals (silicates and phyllosilicates) and the organic matter.

2. Materials and Methods

2.1. Samples

Among the 15 IDPs studied in Maupin et al. (2020), eight have been used in the present work. The seven others have not been used because one of them was returned to NASA (W7068C2), W7068C40 had no infrared signatures, L2076C29 was lost during transfer, and the others were impossible to extract from silicon oil despite several washes with hexane.

We also used micrometric grains from the matrix of four meteorites to investigate different reflectance levels (dark and bright) and heterogeneous compositions. The meteorites have been analyzed in the form of powder prepared in an agate mortar. The obtained powder has not been sieved in order to better simulate the regolith present on the surface of small bodies (Beck et al. 2012). The characteristics of the studied samples are given in Table 1 and the reflectance spectra of the investigated IDPs are given in Figure 1.

Frontier Mountain 95002 (FRO95002 in the following) is a carbonaceous chondrite (CO3). The average carbon content of CO meteorites is approximately 0.6 wt% (Pearson et al. 2006). Reflectance spectra of this meteorite show a slight silicate absorption band in the Vis–NIR range.

Allende is a carbonaceous chondrite (CV3) with 0.3 wt% carbon content (Pearson et al. 2006). Reflectance spectra of this meteorite are characterized by a slight silicate absorption band.

Murchison is a carbonaceous chondrite (CM2) with 2.70 wt% carbon content (Pearson et al. 2006). Reflectance spectra of this meteorite are characterized by a low reflectance level and show a phyllosilicate absorption band around 0.7 μm.

Tagish Lake is an ungrouped meteorite close to CI and CM chondrites with a high carbon content, 5.5 wt% (Grady et al. 2002). Reflectance spectroscopy of this meteorite is characterized by a featureless spectrum with a positive spectral slope in the Vis–NIR. Hiroi et al. (2001) proposed a possible D-type asteroid parent body for the Tagish Lake meteorite. Besides all these samples, we also analyzed the silicon oil used by NASA for the IDPs collection in the stratosphere, in the same conditions and with the same analytical techniques as those used for the IDPs.

2.2. Experimental Techniques

The IDPs previously analyzed by Vis–NIR reflectance spectroscopy (Maupin et al. 2020) have been transferred and crushed in diamond compression cells following the protocol

described in Brunetto et al. (2011) to perform IR spectroscopy. The main advantage of the crushing is the reduction of the scattering effects in the complex three-dimensional aggregate microstructure of the sample, allowing thus an increase of the signal-to-noise ratio and leading to a more precise identification of the different components in the sample (Raynal et al. 2000). Even if this sample preparation leads to the loss of the three-dimensional structure, it preserves the spatial relationships at scales $< 3\,\mu$m and it does not cause any chemical or molecular alterations to the individual grains (Brunetto et al. 2011). IR and Raman microspectroscopy have been performed on the samples crushed in diamond cells.

The Vis–NIR reflectance microspectroscopy in the range 0.45 to 1.0 μm was performed using a grating spectrometer Maya2000 Pro (Ocean Optics) with 4.5 nm spectral resolution coupled to a macroscope (Leica Z16 APO) in a clean room at the IAS laboratory (Orsay, France). The sample is unilaterally illuminated (at 45°) by a 1000 μm diameter fiber that is coupled to a halogen source. A Vis–NIR optical fiber (50 or 100 μm in diameter) was positioned orthogonally to the sample in order to collect the light diffused by the sample (at 0°). The collection spot is adjusted to the particle size, and by performing 20 successive rotations of 18° each, we ensure an illumination of the whole particle surface. We thus averaged the 20 spectra to obtain the reflectance spectrum of an isolated particle (see Maupin et al. 2020 for more details).

In the case of measurements performed on the powder (meteorites), an illumination at 45° with a 1000 μm diameter optical fiber is used and the light reflected by the sample is collected at 0° by an optical fiber of 100 μm in diameter; a collection spot size of about 3 mm is used. This spot size is large enough to take into account the whole heterogeneity of the samples.

We performed IR analysis at the SMIS (Spectroscopy and Microscopy in the Infrared using Synchrotron) beamline of the French synchrotron SOLEIL with a Thermo-Fischer Continuum coupled to an MCT (mercury–cadmium–tellurium) detector cooled with liquid nitrogen, we obtained spectra in the range (4000–700 cm^{-1} or 2.5–14.3 μm). We measured all our spectra in transmission mode using the internal Globar source or the synchrotron source with a spatial resolution adapted to the sample size (with a Schwarzschild–Cassegrain objective ×32 with numerical aperture of 0.65) and with a spectral resolution of 4 cm^{-1}.

Raman microspectroscopy was performed using a DXR Raman spectrometer from Thermo Fisher with a 532 nm exciting laser radiation focused with an objective ×100 with a numerical aperture of 0.8 on a 0.7 μm spot. The low laser power ($\leqslant$0.1mW), prevents any chemical modification of the sample (Brunetto et al. 2011). Raman spectra were acquired with a spectral resolution of 4 cm^{-1}. To encompass the heterogeneity of the sample we averaged the spectra obtained at different locations on the sample surface.

3. Spectral Analyses

3.1. IR Features

To analyze the silicate SiO stretching mode around 1000 cm^{-1} (10 μm), we applied the procedure developed by Merouane et al. (2014) to obtain the silicate composition of each particle with an error of ~5%. This procedure consists of a numerical linear combination of IR spectra of standards to fit

the 1000 cm^{-1} feature after a local linear baseline correction in the 800 cm^{-1} to 1280 cm^{-1} range and a normalization to the maximum absorbance in this range. The best fit is obtained by minimizing the χ^2 value. To do so, we used different spectra of silicates and phyllosilicates commonly found in IDPs thanks to the spectral library from Salisbury et al. (1987). We also used spectra of some analogs prepared in our laboratory in the same conditions as the IDPs (i.e., crushed in diamond cells). The used standards were:

1. Fe and Mg end members of olivine (forsterite: Mg_2SiO_4 and fayalite: Fe_2SiO_4). Mg end member and CaMg solid solution of pyroxene (enstatite: $MgSiO_3$ and diopside: $CaMgSi_2O_6$).
2. Amorphous compounds of Fe and Mg olivine-like compositions and an amorphous compound of pyroxene-like Mg composition.
3. Phyllosilicates of the smectite (like saponite, montmorillonite...) and serpentine (like antigorite, chrysotile...) groups.

The aliphatic organic matter CH stretching feature in the 3050–2800 cm^{-1} (3.27–3.57 μm) range is composed of four characteristic bands due to the symmetric and assymmetric stretching modes of the CH$_3$ groups at ~2870 and ~2950 cm^{-1}, respectively, and of the CH$_2$ groups at ~2850 and ~2930 cm^{-1}, respectively, and a feature at around 2900 cm^{-1} (3.45 μm) that can be attributed to a Fermi resonance (Dartois et al. 2005).

To compare the amount of carbon in the aliphatic CH in the different samples, we calculated the column density ratio of the CH and the SiO bands noted in the following $N(CH)/N(SiO)$.

The column density of the absorption band of the x group $N(x)$, given in molecules. cm^{-2}, is defined as:

$$N(x) = \int_{\text{band}} \frac{\tau_\nu d\nu}{A_x}$$

were τ_ν is the optical depth ($\ln(T_\nu)$ with T_ν the transmittance) at the wavenumber ν and A_x the band strength in cm molecules^{-1}. The band strengths used for the CH group and for the SiO group vary according to the authors because the value of the band strength depends on the environment of the molecules. Günay et al. (2018) obtained on synthetized analogs of interstellar carbon grains a value of 4.69×10^{-18} cm molecules^{-1}, while Matrajt et al. (2005) used the value of 1.2×10^{-17} cm molecules^{-1} obtained by dividing the value of the hexane by 6. In the following we choose the value of Günay et al. (2018). For the SiO group we used 2.0×10^{-16} cm molecules^{-1} according to different studies (e.g., Matrajt et al. 2005; Brunetto et al. 2011). We adapt the limits to each absorption band to take into account the variations between each sample and we calculate the column density after a local linear baseline correction.

3.2. Raman Features of Aromatics

The Raman feature of aromatic compounds is between 1600 cm^{-1} and 1200 cm^{-1}, it is composed of 5 bands. The G band, centered at about 1580 cm^{-1}, corresponds to the mode of the ideal graphitic lattice; the D1 band, centered at about 1350 cm^{-1} and the D2 band, centered at about 1620 cm^{-1}, are related to disordered graphitic lattice; the D3 band, centered at
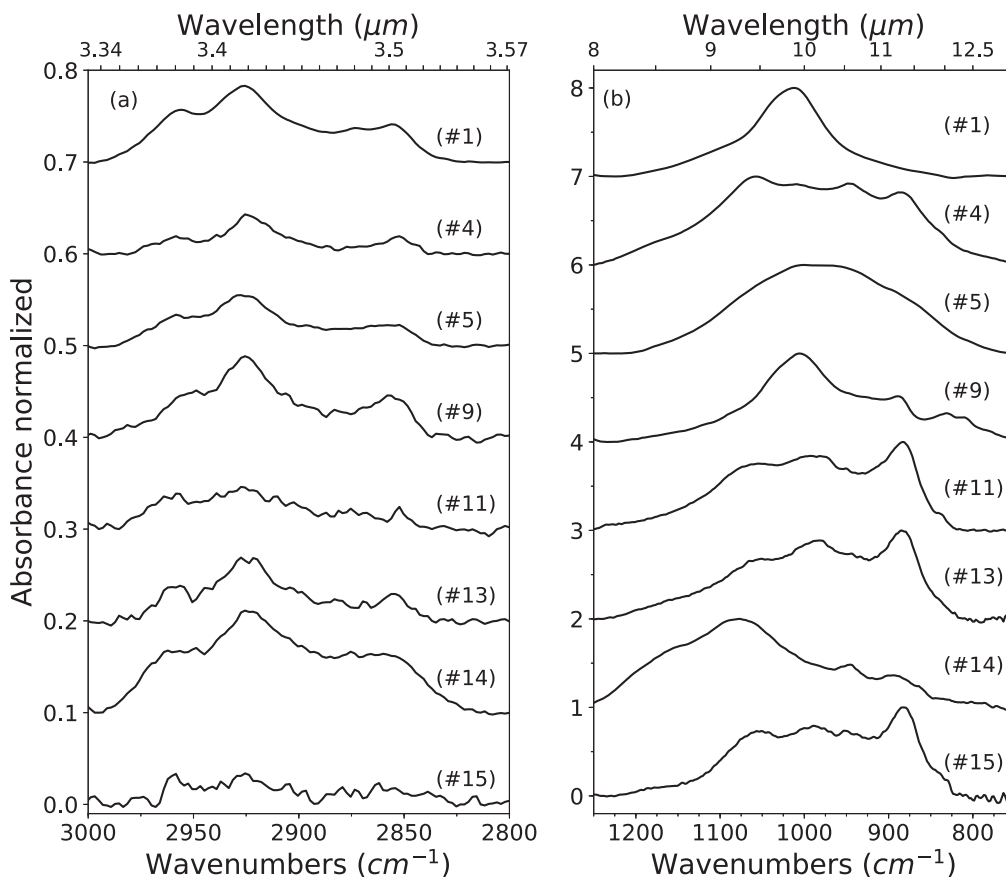
Figure 2. The aliphatic band in the [3000–2800] cm^{-1} range (panel a) and the silicate band in the [1250–750] cm^{-1} range) for each IDP represented by its allocated number. These spectra are first corrected from a local linear baseline, then from the silicon oil contribution and finally normalized to the maximum of the silicate peak. The spectra have been shifted in the absorbance axis for clarity.

about 1500 cm^{-1}, is related to amorphous carbon; the D4 band, centered at about 1200 cm^{-1}, is attributed to disordered graphitic lattice, polyenes and ionic impurities (e.g., Brunetto et al. 2009 and references therein). In our study we can assume that the Raman feature of aromatic organics is composed of two main bands. The so-called D (disorder) and G (graphitic) bands at about 1350 cm^{-1} and 1600 cm^{-1} respectively. Thus, the G band encompasses the G, D2, and part of the D3 bands, and the D band encompasses the D1, D4, and the remaining part of the D3 bands. For each band, after a linear baseline correction between 900 and 1800 cm^{-1}, we used two methods to determine the Raman bands parameters (e.g., band position noted ω and FWHM noted Γ). In the first method, we manually extracted ω_H the Raman shift of the maximum of the band as well as the Raman shift of the half maximum $\omega_{H/2}$ on the left of the G band and on the right of the D band (when the graphs are represented with descendant Raman shifts). Finally, we calculated the FWHM, $\Gamma = 2|\omega - \omega_{H/2}|$.

The second method is based on a procedure that fits the bands with two Lorentzian models; the desired parameters are thus extracted by the automatic procedure. Finally, we averaged the values obtained with the two methods described above and estimated the error ranges of the parameters.

4. Results

4.1. IR Microspectroscopy

The IR spectrum obtained on the silicon oil showed evidence of contamination for all IDPs except two of them, L2071E43

(#11) and W7068B37 (#14). We then performed a contamination experiment on a Tagish Lake grain to develop a method to properly remove the silicon oil contribution from the IDPs' IR spectra (see the Appendix).

Figure 2 shows in panel (a) the aliphatic signatures in the 3000–2800 cm^{-1} range and in panel (b) the silicate feature at ~1000 cm^{-1} (10 μm) in the 1250–750 cm^{-1} range for each studied IDP. The different spectra have been corrected from the baseline and normalized to the maximum peak of the silicate region. For clarity they have been shifted in the vertical axis.

For each IDP, we fitted the 10 μm band (by using the different standards cited above) to infer its mineral composition. The fit procedure was used before and after the spectral correction from the silicon oil contribution. We found in both cases the same composition within 5%. The obtained results are summarized in Table 2. Three IDPs show a hydrated composition, including IDP L2079C18 (#1) who exhibited a typical absorption band of phyllosilicate in its Vis–NIR spectrum (Maupin et al. 2020) as well as a characteristic feature at ~3670 cm^{-1} in its mid-IR spectrum, characteristic of the M–OH in the silicate layer. In our data set the anhydrous IDPs are mostly olivine-rich. The composition of IDP W7068B37 (#14) could not be properly obtained because of the bump at 1120–1220 cm^{-1}. However, several features in its 10 μm band indicate the presence of pyroxene and/or olivine. The shape of this silicate band reminds one of a hydrated IDP having undergone significant heating during atmospheric entry and resulting in an alteration of its composition with a

Table 2
Silicate Composition of the Studied IDPs Inferred from the 10 μm Band

Allocated Number	Phyllosilicate Fraction (%)	Amorphous Fraction (%)	Olivine Fraction (%)	Pyroxene Fraction (%)	ol/(ol+pyr)
1	94	3	3	0	1
4	0	50	15	35	0.3
5	15	80	0	5	0
9	65	0	35	0	1
11	0	30	55	15	0.79
13	0	30	55	15	0.79
14	…	…	…	…	…
15	0	20	55	25	0.69

Note. Silicate composition of the studied IDPs inferred from the 10 μm band fit with an error of about 5% (as explained in the text). The IDP W7068B37 (#14) spectrum fit was inconclusive (see explanation in the text).
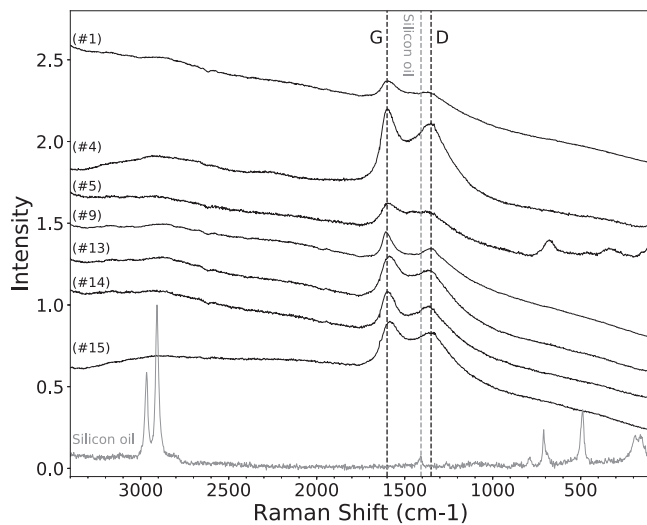
Figure 3. Comparison of the Raman spectra of the studied IDPs, identified by their allocated number, and the silicon oil spectrum. The black dashed lines point out the positions of the G and D bands and the gray dashed line points out the silicon oil feature in the range of interest. The spectra have been shifted in the intensity axis for clarity.

transition from phyllosilicate to anhydrous silicate (Sandford & Bradley 1989; Battandier 2018).

In order to evaluate the carbon richness in the CH aliphatic groups, we calculated the column density ratio of $N(\mathrm{CH})/N$ (SiO) for each IDP. Because of the contamination of silicon oil we first performed a study of this effect on the Tagish Lake meteorite grain (see the Appendix). We calculated the ratio N (CH)/N(SiO) in the three cases: before contamination we found a ratio of 2.17 ± 0.004, after contamination with silicon oil we found a ratio of 2.16 ± 0.004, and finally after spectrum correction from the silicon oil contribution we found a ratio of 2.14 ± 0.004. We thus concluded that the values that we obtained are similar and lie in the range ~ 2.1–2.2. For the studied IDPs, we choose to calculate the average of the ratio with the contaminated spectrum and after correction from the silicon oil contribution to ensure that the two values do not differ too much from each other. The difference between these two values gives the error on this ratio due to the presence of silicon oil σ_{oil}. The error associated with the lower and upper limits of the bands in the calculation of the ratio areas is of the order of $\sigma_l = 0.0001$. The uncertainty associated at each ratio is

Table 3
CH versus SiO in IDPs Based on the IR Bands

Allocated	Area(CH)/Area(SiO)	$N(\mathrm{CH})/N(\mathrm{SiO})$
1	$0.051\,8 \pm 0.0003$	2.21 ± 0.01
4	$0.008\,4 \pm 0.0003$	0.36 ± 0.01
5	$0.016\,7 \pm 0.0004$	0.71 ± 0.02
9	$0.034\,0 \pm 0.0006$	1.45 ± 0.03
11	$0.016\,1 \pm 0.0001$	0.688 ± 0.004
13	$0.020\,7 \pm 0.0007$	0.88 ± 0.03
14	$0.045\,8 \pm 0.0001$	1.952 ± 0.004
15	0.013 ± 0.001	0.55 ± 0.05

Note. The bands' area ratios and the column density ratios of the CH and SiO components.

obtained by $\sqrt{\sigma_{\mathrm{oil}}^2 + \sigma_l^2}$. The obtained results are summarized in the Table 3.

4.2. Raman Microspectroscopy

Figure 3 shows the Raman spectra of silicon oil and IDPs, except for IDPs L2071E43 for which no Raman signatures were obtained (its spectrum is dominated by fluorescence). The silicon oil spectrum has only one weak band at $1407\,\mathrm{cm}^{-1}$ due to the bending modes of the CH_3 functional groups. The features due to the silicon oil around $3000\,\mathrm{cm}^{-1}$ were not detected in any Raman spectrum of IDPs because of the fluorescent background of the spectra in this region. The spectrum of IDP L2071E34 exhibits mineral signatures in the range $[200$–$800]\,\mathrm{cm}^{-1}$ associated to oxides such as magnetite. We summarize in Table 4 the Raman parameters for each studied IDP determined according to the method explained above.

Thermal metamorphism leads to an increase of the order in the aromatic carbonaceous matter (e.g., Moroz et al. 1998 and references therein), the formation of graphite nanocrystals and the disappearance of defects in the graphite grid (Ferrari & Robertson 2000). These changes are reflected in Raman spectroscopy by the increase of ω_G toward values close to $1600\,\mathrm{cm}^{-1}$ due to the appearance of the D2 band at $\sim 1620\,\mathrm{cm}^{-1}$. A more important metamorphism leads to the disappearance of the D2 band inducing a gradual return of ω_G toward smaller values around $1581\,\mathrm{cm}^{-1}$, corresponding to the position of the very thin band of pure graphite (Busemann et al. 2007). The widths of the G and D bands are also indicators of

Table 4
Raman Parameters of the Studied IDPs

Particle	Allocated Number	ω_G (cm^{-1})	Γ_G (cm^{-1})	ω_D (cm^{-1})	Γ_D (cm^{-1})
L2079C18	1	$1\,590.9 \pm 1.5$	98 ± 3	$1\,359.8 \pm 1.6$	285 ± 3
W7068B18	4	$1\,596.4 \pm 1.5$	91 ± 3	$1\,349.7 \pm 1.5$	242 ± 3
L2071E34	5	$1\,589.5 \pm 1.7$	110 ± 3	$1\,357.8 \pm 2.0$	259 ± 3
L2079D12	9	$1\,605.7 \pm 1.5$	57 ± 3	$1\,346.2 \pm 1.6$	247 ± 3
L2071E43	11	…	…	…	…
L2083G23*	13	$1\,582.7 \pm 1.5$	117 ± 3	$1\,358.1 \pm 1.9$	274 ± 3
W7068B37	14	$1\,592.9 \pm 1.5$	92 ± 3	$1\,361.3 \pm 1.7$	266 ± 3
L2083E39	15	$1\,580.1 \pm 1.5$	124 ± 3	$1\,363.2 \pm 1.8$	301 ± 3
Tagish Lake	…	$1\,593.4 \pm 1.5$	92.2 ± 6	$1\,370.5 \pm 1.5$	268 ± 6
Murchisson	…	$1\,595.5 \pm 1.5$	83.8 ± 3	$1\,354.9 \pm 1.6$	243.7 ± 3
Allende	…	$1\,602.1 \pm 1.5$	60.4 ± 3	$1\,348.7 \pm 1.6$	70 ± 3
FRO95002	…	$1\,599.9 \pm 1.5$	66 ± 3	$1\,346.4 \pm 1.8$	91 ± 3

Note. The spectrum of L2071E43 is dominated by fluorescence and no Raman signature was detected.

the disorder of the aromatic matter. The most primitive IDPs are those with the highest values of Γ_D, ω_D and Γ_G and the smallest values of ω_G. These characteristics reflect the disorder of the aromatic carbonaceous material. On the contrary, IDPs with small values of Γ_D and Γ_G and high values of ω_G are more metamorphosed IDPs (Busemann et al. 2007).

We report in Figure 4(a) Γ_G as a function of ω_G for the IDPs and the four meteorites studied here. We find the same trend as the one described for meteorites (Busemann et al. 2007). We then conclude that the most primitive IDPs are those with the smallest ω_G and the highest Γ_G values. Taking into account that the G band encompasses a part of the D band, and that graphitization does not affect the D and G bands in the same way and with the same efficiency (see Figure 2 in Busemann et al. 2007), we plot in Figure 4(b) the total width $\Gamma_G + \Gamma_D$ as a function of the position ω_G.

The IDP L2079D12 (#9) has its G band centered at ($\sim$1605 cm^{-1}), indicating an important graphitization; its D broad band, located at $\sim$1346 cm^{-1} indicates an important contribution of the D4 component (centered at 1200 cm^{-1}). We thus conclude that this IDP underwent a significant graphitization with respect to other IDPs, by its degree of disorder is still somewhat different from CO and CV meteorites whose graphitization stage is more advanced (as probed by their narrower D band). The comparison between Figures 4(a) and 4(b) confirms that samples showing little differences in their Γ_G (e.g., IDP (#9) and meteorites FRO95002 and Allende) can have large differences in their Γ_D and consequently in the parameter $\Gamma_G + \Gamma_D$ that we introduced here. In this respect, the graphitizations of FRO95002 and Allende are more advanced than in any IDP measured here.

5. Discussion

5.1. Organic Matter and Silicate Composition

Figure 5 shows the evolution of the $N(CH)/N(SiO)$ ratio with the phyllosilicates fraction for each IDP. We added to our study the IDPs from the data set of Merouane et al. (2014; represented by light gray symbols). We reanalyzed their data (available in the laboratory) with the method used here. We see that the anhydrous IDPs have a very wide range of variations of the $N(CH)/N(SiO)$ ratio. This is in good agreement with Thomas et al. (1993), who calculated the atomic C/Si ratio in CP-IDPs. Some IDPs have a high carbon content comparable to

those of comets, while some IDPs have low values close to those of CI meteorites (see Figure 7 in Bardyn et al. 2017). This could therefore indicate that the carbon-rich IDPs are of cometary origin while the others could come from asteroids. But this strong variation can also be due to the thermal processing of the IDPs, inducing a destruction of the organic matter and therefore leading to a decrease of their carbon content. This thermal alteration can occur in the parent bodies of the IDPs and/or during their atmospheric entry (Battandier et al. 2018).

For the hydrated IDPs studied here, we observe a linear correlation between the amount of the aliphatic CH groups and the percentage of phyllosilicate in the grain (linear fit in Figure 5 with $R^2 \sim 0.98$). This trend observed in the hydrated IDPs is confirmed by the values of $N(CH)/N(SiO) = 2.17 \pm 0.004$ obtained on the grain of the Tagish Lake meteorite, whose silicate composition was inferred by the same procedure as the IDPs. This dependence may indicate a possible role played by the phyllosilicates in the protection and/or formation of organic matter in hydrated IDPs. It could also indicate the role of organic matter on phyllosilicate formation as reported by Hirakawa et al. (2021). This process occurs on dry meteorites such as meteorites of the CO and CV groups and is therefore associated with significant graphitization of organic matter (e.g., Nakamura 2005; Hirakawa et al. 2021).

Figure 4 shows that IDPs are more pristine than CO and CV meteorites from the point of view of Raman parameters as suggested by previous studies (e.g., Busemann et al. 2009; Starkey et al. 2013; Chan et al. 2020). The hydrated IDPs are closer to the CM Murchison meteorite. The hydration process on CM-type meteorites comes from the melting of the ice contained in the parent body by the heating induced by radioactive decay of the elements with short periods (e.g., Brearley 2006; Merk & Prialnik 2006 and references therein). Liquid water circulation on parent bodies causes the alteration of minerals (hydration) and leads to redistribution and migration of elements (Brearley 2006; King et al. 2017; Hirakawa et al. 2021). Yesiltas & Kebukawa (2016) also showed a correlation between organic matter and phyllosilicates in grains of the Tagish Lake meteorite (based on the OH band at 3050 cm^{-1}) and concluded that phyllosilicates can play a role in the formation and/or protection of organic matter in the parent body. Flynn et al. 2003, 2008) studied anhydrous and hydrated IDPs and did not observe a difference in the bulk
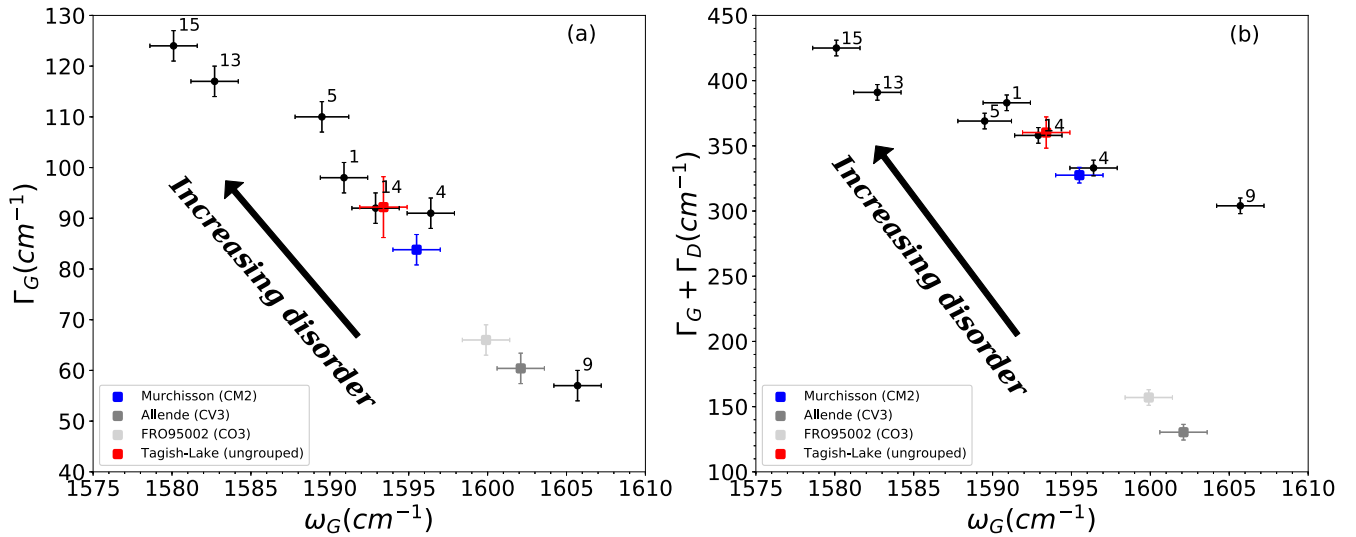
Figure 4. Panel (a) Γ_G as a function of ω_G for the studied IDPs (represented by the the black points and their corresponding allocated number), and the meteorites Murchison (blue square), Allende (gray square), Tagish Lake (red square), and FRO95002 (light gray square). Panel (b) $\Gamma_G + \Gamma_D$ in function of ω_G for IDPs (black points), Murchison (blue square), Allende (gray square), Tagish Lake (red square), and FRO95002 (light gray square) meteorites.
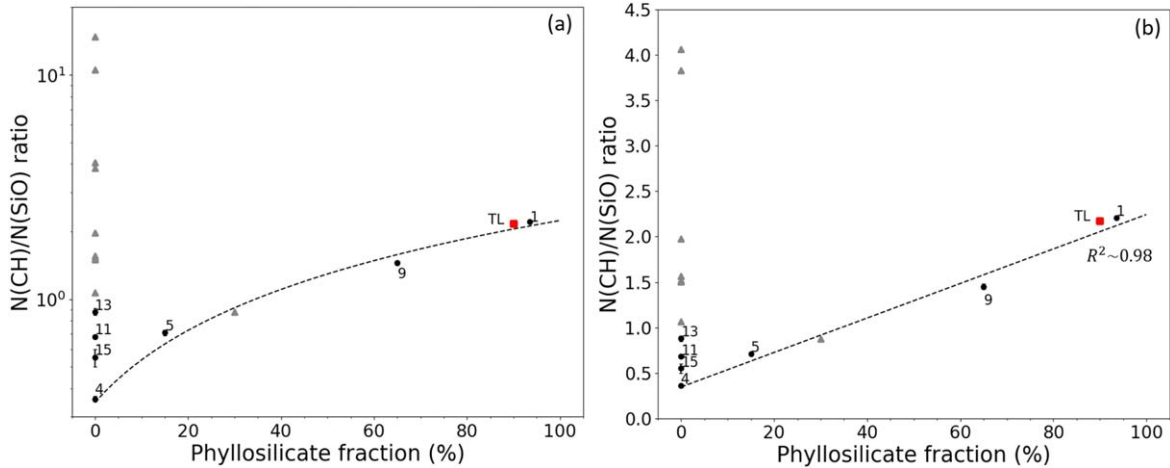
Figure 5. The $N(CH)/N(SiO)$ ratio vs. the phyllosilicate fraction in IDPs. The light gray symbols are the IDPs from Merouane et al. (2014). The red square shows the value obtained on a grain of the Tagish Lake (TL). The error on the phyllosilicate fraction is about 5%. The dashed line is a linear adjustment of the trend observed on hydrated materials. Note that the vertical axis is in log-scale in panel (a). Panel (b) shows the linear increase of the $N(CH)/N(SiO)$ ratio with the phyllosilicate fraction in the hydrated IDPs.

of organic matter between the two groups. They concluded that most of the organic matter was formed before aqueous alteration in the parent bodies and that this process did not significantly alter the bulk of the organic matter. Thus, the correlation observed in our study between organic matter and phyllosilicates in IDPs seems to result from a process of enrichment (migration and/or redistribution) or of protection of the organic matter during aqueous alteration on the parent bodies as suggested by previous studies (e.g., Flynn et al. 2003, Flynn et al. 2008; Yesiltas & Kebukawa 2016; Dionnet et al. 2018; Vinogradoff et al. 2020 and references therein).

5.2. Organic Matter and the Reflectance Level

IDPs are dark materials and can be linked to very primitive bodies in the solar system (e.g., Bradley et al. 1996; Vernazza et al. 2015). The lowest albedo of some primitive small bodies is often associated with the presence of polyaromatic carbonaceous refractory material and/or sulfides (Quirico

et al. 2016). The low reflectance in the visible range can also be explained by an effect of grain size components on the surface (Greenberg 1986). To study the influence of organic matter present in dark materials, we consider the IDPs and the Allende, Murchison, and Tagish Lake meteorites with reflectance levels <10%. Figure 6 shows the reflectance level as a function of the ratio N(CH)/N(SiO). The points on this figure show a very weak correlation, which seems stronger only for the three hydrated IDPs (#1, 5 and 9), suggesting that the amount of carbon in the aliphatic CH does not influence much the reflectance level of the object, except possibly for hydrated IDPs. This can be explained by the relatively low absorbance in the visible range of aliphatics (Jones 2012) and/or by the fact that CH components are mainly contained inside the grain (Flynn et al. 2003). Indeed, IDPs are very dark in the visible range and the photons could probe only the surface of the sample in reflectance measurements. On the contrary polyaromatic organic matter has efficient absorption in the visible due
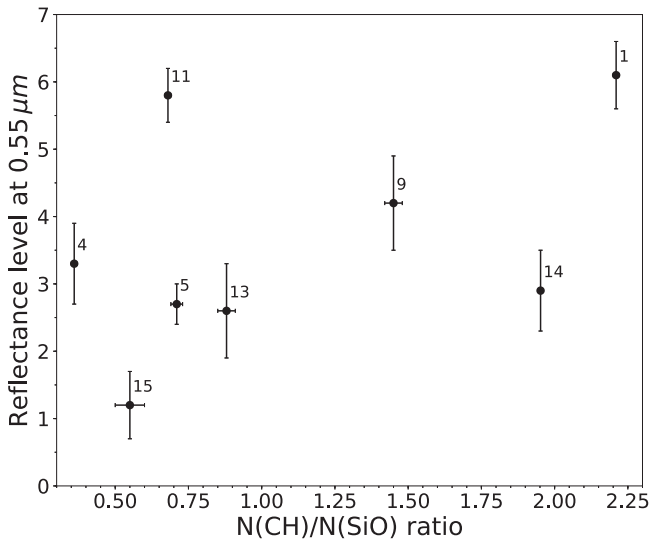
Figure 6. Reflectance level at 0.55 μm of the IDPs as a function of the N(CH)/N(SiO) ratio.

to the $\pi - \pi^*$ electronic transition (e.g., Moroz et al. 1998 and references therein). Figure 7(a) shows the reflectance levels as a function of the position of the G band (ω_G) which characterizes the degree of graphitization of the aromatic material. We obtain a clear trend for the most primitive objects (IDPs, Tagish Lake and Murchison), except for IDP L2079C18 (#1) which seems out of the trend. This IDP is particular from the point of view of its composition with a very high degree of hydration, similar to Tagish Lake (see panel (b) in Figure 5). Its Vis–NIR spectrum is dominated by phyllosilicates absorption with a very marked absorption band around 0.66 μm (depth of 8% relative to the continuum, see Maupin et al. 2020). Its Raman D and G bands are relatively weaker than other IDPs and than Tagish Lake, which might suggest its polyaromatic content is relatively low. Therefore its spectral properties in the Vis–NIR could be dominated by phyllosilicates and not by organic matter. Another possibility is the potential space weathering on IDP L2079C18 (#1) which would have produced a modification of the G and D bands of the polyaromatic material, such as an increase in the bandwidths and a raise or decrease of the reflectance level (Lantz et al. 2015, 2017). This point remains open for future investigations. For the other IDPs (4, 5, 9, 13, 14, and 15) and the Tagish Lake and Murchison meteorites we see that the reflectance level increases with an increasing graphitization of the polyaromatic material. For highly processed materials, the G band goes back to low wavenumbers (1580 cm^{-1}) which may explain the reverse alignment of the Allende meteorite (gray diamond in Figure 7(a)). As seen previously, the position of the G band shows the graphitized character of the polyaromatic material but does not fully reflect the degree of order of the polyaromatic material. Figure 7(b) shows the evolution of the reflectance level as a function of $\Gamma_G + \Gamma_D$. If we disregard the IDP L2079C18 (#1), as discussed before, it appears a linear correlation (linear fit with $R^2 \sim 0.99$). From this linear trend we propose that:

1. the polyaromatic organic matter controls the reflectance level for dark materials.
2. the reflectance level increases with graphitization and especially with increasing order in the graphitic lattice.

Our findings are in good agreement with Quirico et al. (2016) and Sultana et al. (2021) who showed that the darkest characteristics of some small bodies implies the presence of an absorbing constituent, like organic material, on their surface. We suggest here the presence of abundant polyaromatic organic matter.

5.3. Implications for Remote Sensing and Sample Return Missions

Reflectance spectroscopy in the Vis–NIR range is the most widely used technique for the observation of small bodies. However the spectrum in the Vis–NIR is not sufficient to obtain precise information on the composition of the target body. The lack of characteristic absorption bands makes comparison between laboratory and remote sensing spectra difficult. We show here that the reflectance level is a very sensitive parameter to probe the polyaromatic component of a primitive dark surface. With the reflectance level, we can obtain an indication of the polyaromatic units contained in the surface, as the graphitization degree and the degree of order in the polyaromatic matter. This information could be used for the two current asteroid sample return missions: Hayabusa2 with target Ryugu and OSIRIS-REx with target Bennu. Ryugu is a very dark C-type asteroid with reflectance level at 0.55 μm of $1.88 \pm 0.17\%$ (Sugita et al. 2019; Watanabe et al. 2019). The very low reflectance level could be an indication of a very primitive surface with bulk organic matter poorly graphitized and with a high degree of disorder. Bennu is a dark B-type asteroid with reflectance level at 0.55 μm of $\sim 2\%$ (Hamilton et al. 2019). If we apply our results to these two asteroids, we can conclude that there are similarities in the bulk polyaromatic organic matter of Ryugu and Bennu and that their polyaromatic units could be closer to those of the IDPs and CM meteorite and not of the CV and CO meteorites.

Ryugu could have undergone a process of dehydration very early in its history (Kitazato et al. 2021) while Bennu's hydration which could have taken place in large quantities (Hamilton et al. 2019; Kaplan et al. 2020). Kitazato et al. (2021) showed that Ruygu's dehydration took place at a relatively low temperature between 300 °C and 700 °C. Based on the reflectance level, we can expect the polyaromatic units on Ruygu to be relatively primitive, therefore not graphitized. Based on heating experiments performed on polyaromatic materials (e.g., Dillon et al. 1984) a maximum temperature can be estimated. The maximum temperature so that the polyaromatic material does not undergo a major change in its structure could thus be between 500 °C and 600 °C. This result is consistent with that of Kitazato et al. (2021) and thus confirms that Ryugu underwent a low-temperature dehydration process. The experiments carried out soon on the samples collected on these two asteroids will thus be able to confirm our results.

The JWST will be launched in 2021 December; besides all its other goals, it will observe the solar system small bodies in the near-IR and mid-IR ranges with enough sensitivity to observe dark surfaces. Thus, new data will soon be available on asteroid surfaces. Our results can provide support for interpreting these future observations, in particular about the relationship between organic matter and hydration.
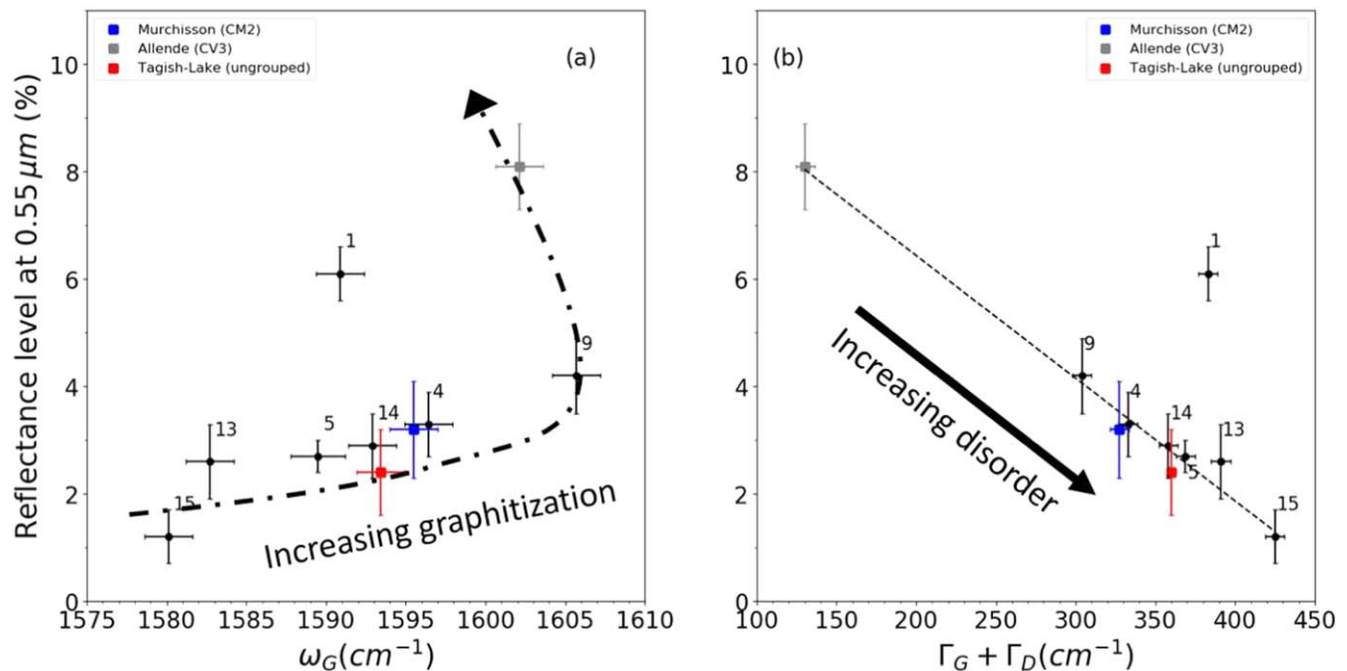
Figure 7. (a) Reflectance level at 0.55 μm of IDPs, Murchison (blue square), Allende (gray square), and Tagish Lake (red square) meteorites as a function of the ω_G parameter. (b) Reflectance level at 0.55 μm in function of the width of the $G+D$ band for IDPs (black points) and Murchison (blue square), Allende (gray square), and Tagish Lake (red square) meteorites.

6. Conclusion

Our study suggests that the reflectance level in the visible of the extraterrestrial materials is mainly controlled by polyaromatic organic matter and could be an indicator of the nature of the organic matter. In particular, the reflectance level is sensitive to the degree of graphitization and degree of order of the polyaromatic organic matter.

We have shown that collected extraterrestrial materials containing primitive polyaromatic organic matter (with a high degree of disorder and low graphitization) are the darkest. This result provides important information on the potential explanation for the low reflectance level of some bodies, in particular for D-type asteroids and comets. Some studies attempt to explain this low reflectance in the visible by the effect of grain size. We show here that the reflectance level in the visible is mainly controlled by the state of the polyaromatic organic matter (graphitization and degree of order).

We show also that the aliphatic matter does not play a role in the reflectance level of dark surfaces and the amount of aliphatic organic matter is strongly correlated with the degree of hydration. We interpret this effect as a result of the aqueous alteration on the parent body.

Appendix
Correction of the Silicon Oil Contribution in the IR Spectra of IDPs

The infrared spectrum of the silicon oil used by NASA for the IDP collection is given in Figure 8. This spectrum, acquired in the same conditions as those of the studied IDPs, is normalized to the band 800 cm^{-1} which is the most intense. In the upper panel of Figure 8 we also present the IR spectra of the studied IDPs normalized to their silicate band. All spectra have been shifted in the vertical axis for clarity. The two bands at 800 and 1261 cm^{-1} are used as indicators of the presence of silicon oil in the IDP's IR spectra. We found that except L2071E43 (#11) and W7068B37 (#14) all IDPs exhibit silicon oil bands in their spectra. Note that silicon oil also has a relatively strong band at $\sim$2963 cm^{-1} which could influence the intrinsic aliphatic features of the IDPs.

In order to investigate the effect of the contamination by silicon oil and to develop an analytical method to correct the IR spectra of IDPs from the silicon oil contribution, we intentionally contaminated a grain of Tagish Lake meteorite with silicon oil. The IR spectra obtained on the Tagish Lake grain before and after contamination are shown in Figure 9. We also superimposed on the spectra the silicon oil signatures in the aliphatic range (panel a) and in the silicate range (panel b). Panel (a) in Figure 9 shows a clear modification of the organic band with an increase of the asymmetric CH$_3$ band in the contaminated Tagish Lake grain. Note the appearance of the 1261 cm^{-1} as well as the 800 cm^{-1} bands in the silicate region (panel b). The silicate band is also modified with a shoulder
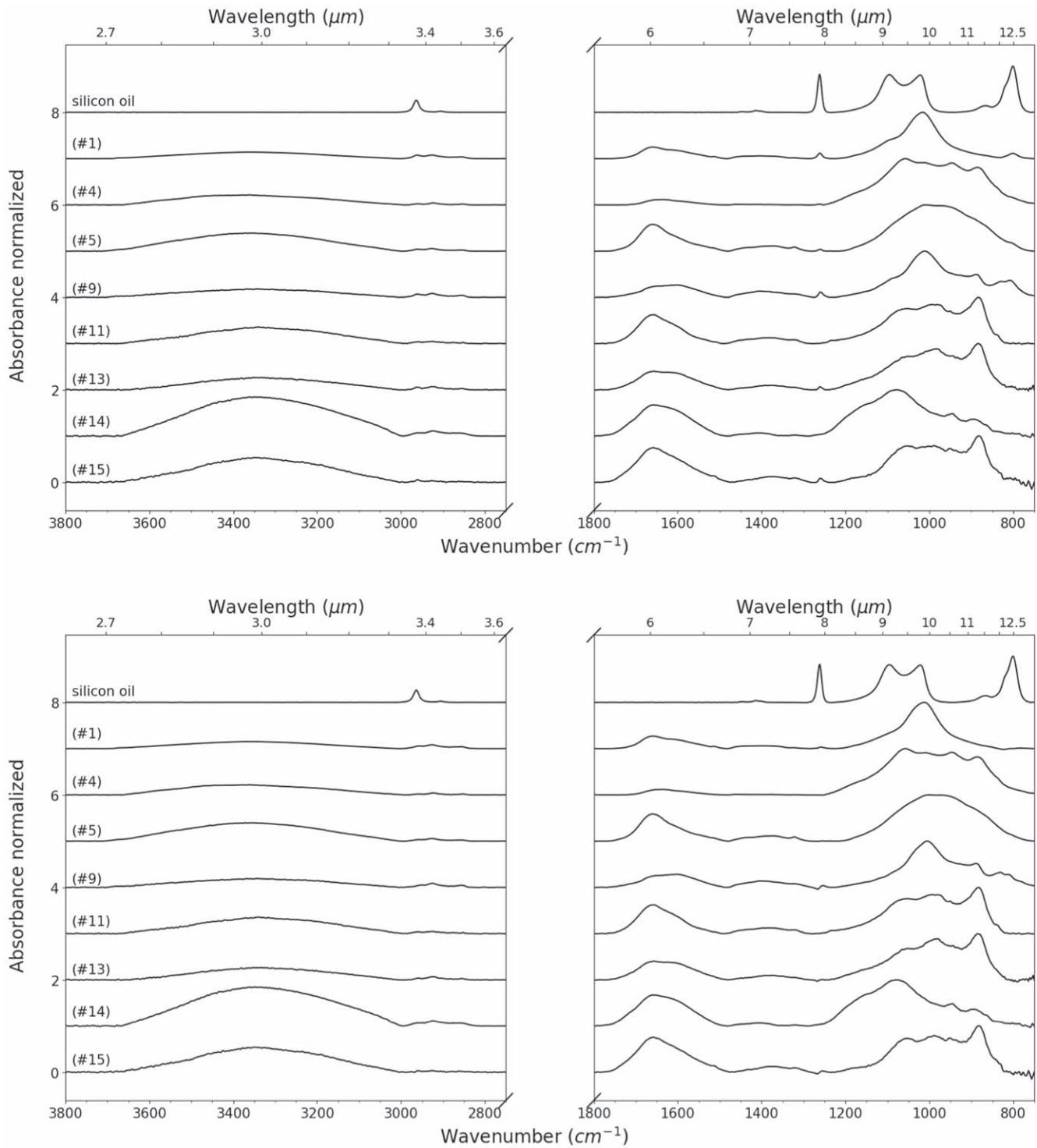
Figure 8. IR spectra of IDPs and silicon oil. The upper spectrum in each panel is the one of the silicon oil obtained after normalization to the 800 cm^{-1} band. The other spectra are those of IDPs; they are normalized to the maximum of the silicate feature. The identification of each IDP is given above its spectrum. The spectra have been shifted in the vertical axis for clarity. The two bottom panels show the same spectra corrected from the silicon oil contribution.

that appears around 1100 cm^{-1}. To remove the silicon oil contribution we chose to apply a linear correction based on either the band at 800 cm^{-1} or on the band at 1261 cm^{-1} according to the band ratios observed in the spectrum. In the

case of the Tagish Lake grain we see that the spectrum after correction shows the same characteristics as the uncontaminated spectrum; see panels (c) and (d) for the aliphatic and silicate regions, respectively. We thus applied the same
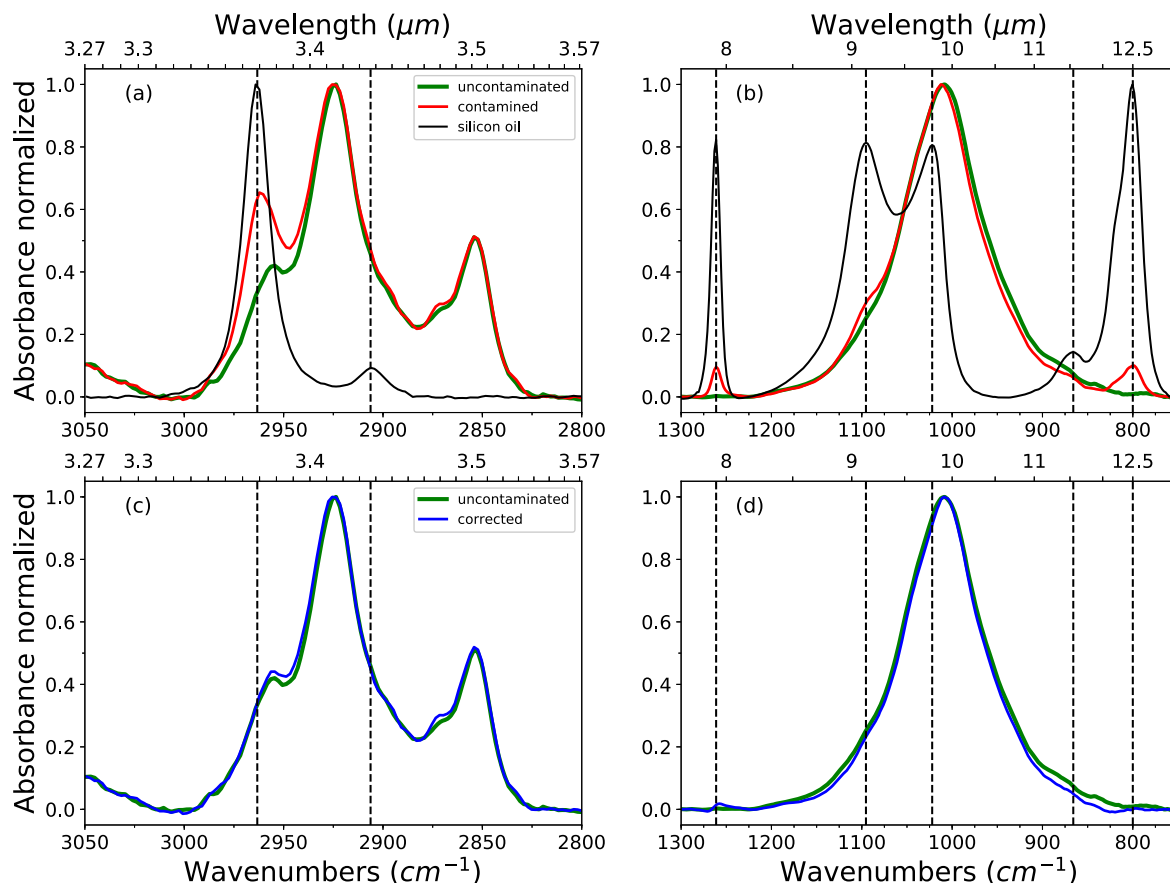
Figure 9. Panels (a) and (b) show the spectra of the silicon oil (black), the uncontaminated Tagish Lake grain (green) and the contaminated Tagish Lake (red) in the aliphatic and silicate regions, respectively. In panels (c) and (d) we compare the uncontaminated Tagish Lake spectrum (green) to the one obtained after a linear correction of the contaminated grain spectrum from the silicon oil contribution in the aliphatic and silicate bands, respectively.

procedure for all contaminated IDPs; the spectra of IDPs before and after correction are shown in the upper and lower panels of Figure 8.

ORCID iDs

Romain Maupin https://orcid.org/0000-0001-8985-0033
Rosario Brunetto https://orcid.org/0000-0003-3001-9362

References

Bardyn, A., Baklouti, D., Cottin, H., et al. 2017, MNRAS, 469, S712
Battandier, M. 2018, PhD thesis, Communauté Université Grenoble Alpes
Battandier, M., Bonal, L., Quirico, E., et al. 2018, Icar, 306, 74
Beck, P., Pommerol, A., Thomas, N., et al. 2012, Icar, 218, 364
Bradley, J. P. 2003, TrGeo, 1, 689
Bradley, J. P., Keller, L. P., Brownlee, D. E., et al. 1996, M&PS, 31, 394
Brearley, A. J. 2006, in Meteorites and the Early Solar System II, ed.
    D. S. Lauretta & H. Y. McSween, Jr. (Tucson, AZ: Univ. Arizona
    Press), 584
Brunetto, R., Borg, J., Dartois, E., et al. 2011, Icar, 212, 896
Brunetto, R., Pino, T., Dartois, E., et al. 2009, Icar, 200, 323
Busemann, H., Alexander, M. O., & Nittler, L. R. 2007, M&PS, 42, 1387
Busemann, H., Nguyen, A. N., Cody, G. D., et al. 2009, E&PSL, 288, 44
Chan, Q. H. S., Franchi, I. A., Zhao, X., et al. 2020, M&PS, 55, 1320
Clemett, S. J., Maechling, C. R., Zare, R. N., et al. 1993, Sci, 262, 721
Dartois, E., Muñoz Caro, G. M., Deboffle, D., et al. 2005, A&A, 432, 895
Dillon, R. O., Woollam, J. A., & Katkanant, V. 1984, PhRvB, 29, 3482
Dionnet, Z., Aleon-Toppani, A., Baklouti, D., et al. 2018, M&PS, 53, 2608
Dumas, C., Owen, T., & Barucci, M. A. 1998, Icar, 133, 221
Ferrari, A. C., & Robertson, J. 2000, PhRvB, 61, 14095

Flynn, G. J., Keller, L. P., Feser, M., et al. 2003, GeCoA, 67, 4791
Flynn, G. J., Keller, L. P., Wirick, S., et al. 2008, in IAU Symp. 251, Organic
    Matter in Space (Cambridge: Cambridge Univ. Press), 267
Goto, M., Maihara, T., Terada, H., et al. 2000, A&AS, 141, 149
Grady, M. M., Verchovsky, A. B., Franchi, I. A., et al. 2002, M&PS, 37,
    713
Greenberg, J. M. 1986, Natur, 321, 385
Günay, B., Schmidt, T. W., Burton, M. G., et al. 2018, MNRAS, 479, 4336
Hamilton, V. E., Simon, A. A., Christensen, P. R., et al. 2019, NatAs, 3, 332
Hirakawa, N., Kebukawa, Y., Furukawa, Y., et al. 2021, EP&S, 73, 16
Hiroi, T., Zolensky, M. E., & Pieters, C. M. 2001, Sci, 293, 2234
Jones, A. P. 2012, A&A, 545, C2
Kaplan, H. H., Lauretta, D. S., Simon, A. A., et al. 2020, Sci, 370, eabc3557
King, A. J., Schofield, P. F., & Russell, S. S. 2017, M&PS, 52, 1197
Kitazato, K., Milliken, R. E., Iwata, T., et al. 2021, NatAs, 5, 246
Lantz, C., Brunetto, R., Barucci, M. A., et al. 2015, A&A, 577, A41
Lantz, C., Brunetto, R., Barucci, M. A., et al. 2017, Icar, 285, 43
Love, S. G., & Brownlee, D. E. 1993, Sci, 262, 550
Martins, Z., Chan, Q. H. S., Bonal, L., et al. 2020, SSRv, 216, 54
Matrajt, G., Messenger, S., Brownlee, D., et al. 2012, M&PS, 47, 525
Matrajt, G., Muñoz Caro, G. M., Dartois, E., et al. 2005, A&A, 433, 979
Maupin, R., Djouadi, Z., Brunetto, R., et al. 2020, PSJ, 1, 62
Merk, R., & Prialnik, D. 2006, Icar, 183, 283
Merouane, S., Djouadi, Z., & Le Sergeant d'Hendecourt, L. 2014, ApJ,
    780, 174
Moroz, L. V., Arnold, G., Korochantsev, A. V., et al. 1998, Icar, 134, 253
Muñoz Caro, G. M., Matrajt, G., Dartois, E., et al. 2006, A&A, 459, 147
Nakamura, T. 2005, JMPeS, 100, 260
Pearson, V. K., Sephton, M. A., Franchi, I. A., et al. 2006, M&PS, 41, 1899
Quirico, E., Moroz, L. V., Schmitt, B., et al. 2016, Icar, 272, 32
Raynal, P. I., Quirico, E., Borg, J., et al. 2000, P&SS, 48, 1329
Rietmeijer, F. 1998, Reviews in Mineralogy, Vol. 36 (Blacksburg, VA:
    Mineralogical Society of America), 95

Salisbury, J. W., Walter, L. S., & Vergo, N. 1987, Mid-infrared Spectroscopic Investigation NASA TM-89810, NASA, 196

Sandford, S. A., & Bradley, J. P. 1989, Icar, 82, 146

Starkey, N. A., Franchi, I. A., & Alexander, C. M. O. 2013, M&PS, 48, 1800

Sugita, S., Honda, R., Morota, T., et al. 2019, Sci, 364, 252

Sultana, R., Poch, O., Beck, P., et al. 2021, Icar, 357, 114141

Thomas, K. L., Blanford, G. E., Keller, L. P., et al. 1993, GeCoA, 57, 1551

Vernazza, P., & Beck, P. 2016, in Planetesimals: Early Differentiation and Consequences for Planets, ed. L. T. Elkins-Tanton & B. P. Weiss (Cambridge: Cambridge Univ. Press)

Vernazza, P., Marsset, M., Beck, P., et al. 2015, ApJ, 806, 204

Vinogradoff, V., Le Guillou, C., Bernard, S., et al. 2020, GeCoA, 269, 150

Watanabe, S., Hirabayashi, M., Hirata, N., et al. 2019, Sci, 364, 268

Yesiltas, M., & Kebukawa, Y. 2016, M&PS, 51, 584